Liquid-state NMR simulations of quantum many-body problems

C. Negrevergne,[1,*] R. Somma,[2,3] G. Ortiz,[2] E. Knill,[4] and R. Laflamme[1]

[1]*Institute for Quantum Computing, University of Waterloo, Waterloo, ON, Canada N2L 3G1*
[2]*Los Alamos National Laboratory, Los Alamos, New Mexico 87545, USA*
[3]*Centro Atómico Bariloche and Instituto Balseiro, 8400 San Carlos de Bariloche, Argentina*
[4]*Mathematics and Computer Sciences Division, National Institute of Standards and Technology, Boulder, Colorado 80305, USA*

Recently developed quantum algorithms suggest that in principle, quantum computers can solve problems such as simulation of physical systems more efficiently than classical computers. Much remains to be done to implement these conceptual ideas into actual quantum computers. As a small-scale demonstration of their capability, we simulate a simple many-fermion problem, the Fano-Anderson model, using liquid-state nuclear magnetic resonance (NMR). We carefully designed our experiment so that the resource requirement would scale up polynomially with the size of the quantum system to be simulated. The experimental results obtained give us an insight to the quantum control required when simulating quantum systems with NMR techniques. The simulation of other physical systems, with different particle statistics, is also discussed.

I. INTRODUCTION

Quantum-mechanical systems provide resources to solve problems which are difficult to solve on classical computers. If we had a large quantum computer today, we could break cryptographic codes [1], perform a variety of search algorithms [2,3], estimate eigenvalues of operators [4,5], or simulate quantum systems [6]. In particular, the latter would enable a better understanding of the quantum world by enabling analysis of complex chemical reactions or demonstrating new states of matter. However, questions like "what are the physical quantum states that can be reached efficiently" or "what kind of physical processes can be efficiently simulated on a quantum computer" still remain open.

Since Richard P. Feynman conjectured that an arbitrary discrete quantum system may be *simulated* by any other [6], the simulation of quantum phenomena became a fundamental problem that a quantum computer, i.e., a universally controlled quantum system, may potentially solve in a more efficient way than a classical computer. Quantum simulation is the process of faithfully imitating a physical phenomenon using a quantum computer. The basic idea is to imitate the evolution of a physical system by cleverly controlling the evolution of the quantum computer. Although Feynman's illuminating conjecture seems appealing, it was only recently proved generally valid [7–11]. Experimentally demonstrating that one has universal control and thus can quantum imitate an arbitrary physical process constitutes an extremely challenging enterprise.

It is important to notice that the efficiencies of quantum simulating the evolution of a physical system and of obtaining the sought-after information about a physical property must be established separately in most cases. A demonstration that evolution can be simulated efficiently [8,10–12], that is, can be simulated with polynomial resources as a function of problem size, is in general insufficient for showing that the desired property (e.g., the ground-state energy of a given Hamiltonian) can also be obtained efficiently. In general, arguments based on the exponential size of the Hilbert space of the system to be simulated and the inherent quantum parallelism of a quantum computer are insufficient for showing that an algorithm for quantum computation efficiently solves a problem. We pointed out in Refs. [8,10] that in a quantum computation it is necessary to demonstrate, in addition to maintaining adequate accuracy (noise, approximations, and statistical error control), the polynomial scaling of the amount of resources required to perform the three main steps of a simulation: initialization, propagation, and measurement.

Some quantum processes can be simulated very well and efficiently on classical computers. Simulating quantum phenomena using stochastic approaches reduces the problem to quadratures, which are multidimensional integrals that can be computed using Monte Carlo techniques. In general, the complexity of deterministic N-dimensional integration is of order $\varepsilon^{-N/\alpha}$ (i.e., exponential in N), where $\varepsilon < 1$ is some stipulated error and α quantifies the smoothness of the integrand. On the other hand, the expected complexity of Monte Carlo integration is of order ε^{-2}, and hence independent of N and α (assuming that the variance of the integrand is finite). The reason for introducing these statistical techniques was to overcome the exponential complexity of deterministic approaches such as the Lanczos method [13]. Realistic models of liquid or solid ^{4}He have been simulated to experimentally measured precision for a few years [14]. Recently developed loop-cluster algorithms allow highly efficient and informative simulation of many quantum spin models of magnetism [15].

An important class of problems for which classical computers have major difficulties is the simulation of interacting Fermionic systems (almost all *large-scale* simulations of fermions are done by the Monte Carlo method). In fact, as noted in Refs. [8,10], Feyman and others prior to him intuited this difficulty. Unless an approximation is made, the

various quantum Monte Carlo algorithms must inevitably sample from a multivariate distribution P that has regions of phase space where it is negative that are comparable to regions where it is positive (because the state function belongs to the totally antisymmetric representation of the permutation group). In general, the nodal hypersurface $P=0$ separating the regions is unknown (an exception being when symmetry considerations alone determine it), making it impossible to solve the problem by independently sampling from each region where P has a definite sign. The sign problem is prohibitive on a classical computer because it results in the variance of measured quantities growing exponentially with the number of degrees of freedom of the system. Still other applications require sampling from a complex-valued distribution P. This occurs, for example, if the simulation is done as a function of real Minkowski time or if time-reversal symmetry is broken. In previous work [8,10], we have discussed how certain sign problems can be overcome using quantum algorithms.

In this paper we describe and experimentally demonstrate the quantum simulation of many-body problems using liquid-state NMR quantum information processors (QIPs) [16]. NMR simulations of other physical systems with a few degrees of freedom can be found in, for example, Refs. [17,18]. The constituents of the system may represent particles with arbitrary exchange statistics and generalized Pauli exclusion principle (such as fermions obeying Fermi statistics), spins, etc. In particular, we show how to efficiently imitate a resonant impurity (localized state) scattering process in a metal (which is made of fermions), using the nuclear spins of a transcrotonic acid molecule. This problem is physically modeled by a Fano-Anderson Hamiltonian [8]. Our results show that the universal control achieved by liquid-state NMR QIPs enables, in principle, efficient simulation of some Fermionic (and other particle statistics) systems, providing relevant information about the particular phenomenon or system of study [19]. In particular, we show how the spectrum of the Fano-Anderson Hamiltonian can be determined.

The paper is organized in the following way: In Sec. II we introduce the conventional model of quantum computation and use it to describe the physics of the liquid-state NMR setting, which can be used as a universal quantum simulator. In Sec. III we present some quantum algorithms for obtaining relevant physical properties of quantum systems satisfying different particle statistics, by mapping the algebras of operators used to describe them onto the spin-1/2 algebra (conventional model). In Sec. IV we introduce the Fermionic Fano-Anderson model, and show how to simulate it with the liquid-state NMR QIP. The experimental implementation of this simulation as well as its results and the conclusions are described in Secs. V and VI, respectively.

II. QUANTUM INFORMATION PROCESSING WITH LIQUID-STATE NMR METHODS

In this section we introduce liquid-state NMR quantum information processing methods, emphasizing the fact that they can be mathematically described in terms of Pauli (spin-
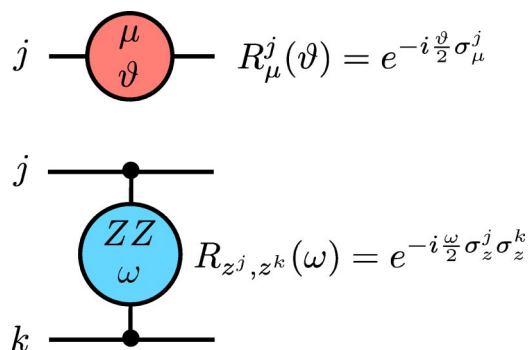

FIG. 1. Circuit representation of the elementary gates. The top picture indicates a single-qubit rotation while the bottom one indicates the two-qubit Ising gate. Any quantum algorithm can be represented by a circuit composed of these elementary gates (see, for example, Fig. 3)

1/2) operators [20]. A more detailed description of such methods can be found in Ref. [16].

In the conventional model of quantum computation the fundamental unit of information is the quantum bit or *qubit*. A qubit's pure state, $|\mathbf{a}\rangle = a|0\rangle + b|1\rangle$ (with $a, b \in \mathbb{C}$ and $|a|^2 + |b|^2 = 1$), is a linear superposition of the logical states $|0\rangle$ and $|1\rangle$, and can be represented by the state of a two-level quantum system such as a spin 1/2. Similarly, a pure state of a register of N qubits (quantum register) is represented as $|\psi\rangle = \sum_{n=0}^{2^N-1} a_n |n\rangle$, where $|n\rangle$ is a product of states of each qubit in the logical basis, e.g., its binary representation ($|0\rangle \equiv |00\cdots0\rangle$, $|1\rangle \equiv |00\cdots01\rangle$, $|2\rangle \equiv |00\cdots10\rangle$, etc.), and $\sum_{n=0}^{2^N-1} |a_n|^2 = 1 (a_n \in \mathbb{C})$. A quantum register can also be in a probabilistic mixture of pure states, i.e., a mixed state, which is described by a density matrix $\rho = \sum_s p_s \rho_s$, with $\rho_s = |\psi_s\rangle\langle\psi_s|$, representing the quantum register being in the pure state $|\psi_s\rangle$, with probability p_s. Every density operator can be written as a sum of products of the Pauli spin-1/2 operators σ_α^j ($\alpha = x, y, z$, and $j = [1, \ldots, N]$) and the identity operators I^j, acting on the jth qubit of the register [16].

The Pauli operators can also be used to describe any unitary operation acting on the state of the register. In particular, every unitary operation can be decomposed in terms of single-qubit rotations $R_\mu^j(\vartheta) = e^{-i(\vartheta/2)\sigma_\mu^j} = [\cos(\vartheta/2)I^j - i\sin(\vartheta/2)\sigma_\mu^j]$, by an angle ϑ around the μ axis, and two-qubit interactions such as the *Ising gate* $R_{z^j,z^k}(\omega) = e^{-i(\omega/2)\sigma_z^j\sigma_z^k} = [\cos(\omega/2)I^jI^k - i\sin(\omega/2)\sigma_z^j\sigma_z^k]$ [21,22], defining a universal set of elementary gates. In Fig. 1 we show the quantum circuit representation of these basic operations.

Finally, in the conventional model of quantum computation the measurement is assumed to be projective and is described by projectors that can also be expanded in terms of Pauli operators.

Liquid-state NMR methods allow us to physically implement a slightly different version of the conventional model of quantum computation, with respect to the initial state and the measurement process. In this setup the quantum register is represented by the average state of the nuclear spin 1/2 of an ensemble of identical molecules. Since all molecules are equivalent, in the following analysis we will first consider only one of them.
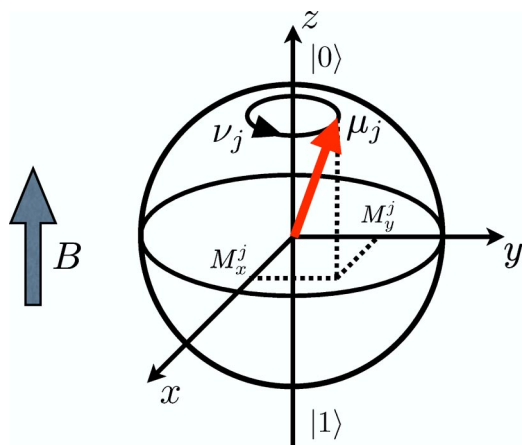
FIG. 2. Bloch's sphere representation of a single nuclear spin-1/2 precessing around the quantization axis determined by the external magnetic field B. The precession frequency is given by $\nu_j = \mu_j B$, with μ_j the magnetic moment of the jth nucleus. Due to the chemical environment, each nucleus precesses at its own Larmor frequency ν_j.

The molecule is placed in a strong magnetic field $B(\hat{z})$ $\simeq 10$ T, so that the spin of the jth nucleus precesses at its Larmor frequency ν_j (Fig. 2). In the frame rotating with the jth spin, its qubit state can then be rotated by sending rf pulses in the x-y plane at the resonant frequency $\nu_r \approx \nu_j$. If the duration of this pulse is Δt, the corresponding evolution operator in the rotating frame is [16]

$$U_j = e^{-iH_j \Delta t} = e^{-iA[\cos(\varphi)\sigma_x^j + \sin(\varphi)\sigma_y^j]\Delta t}, \tag{1}$$

where A is the amplitude of the rf pulse and φ is its phase (i.e., orientation) in the x-y plane ($\hbar = 1$). Then, one can induce single spin rotations [23] around any axis in the x-y plane by adjusting Δt and φ.

Single-qubit rotations around the z axis can be implemented with no experimental imperfection or physical duration simply by changing the phase of the abstract rotating frame we are working with. We have then to keep track of all these phase changes with respect to a reference phase associated with the spectrometer. Nevertheless, these phase tracking calculations are linear with respect to the number of pulses and spins, and can be efficiently done on a classical computer. Together with the rotations around any axis in the x-y plane, the z rotations can generate any single-qubit rotation on the Bloch sphere.

On the other hand, the spin-spin interactions present in the molecule allow us to perform two-qubit gates and achieve universal control. To first order in perturbation, this interaction (called the J coupling), has the form

$$H_{j,k} = \frac{J_{jk}}{4} \sigma_z^j \sigma_z^k, \tag{2}$$

where j, k denote the corresponding pair of qubits and J_{jk} is their coupling strength. Under typical NMR operating conditions, these interaction terms are small enough to be neglected when performing single-qubit rotations with rf pulses of short duration. Nevertheless, between two pulses they are
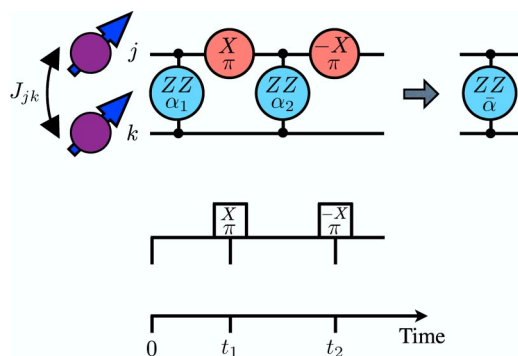

FIG. 3. Circuit representation for the refocusing scheme to control J couplings. The Ising-like coupling J_{jk} between spins can be controlled by performing flips on one of the spins at times $t_1 = \Delta t_1$ and $t_2 = t_1 + \Delta t_2$, respectively. The effective coupling is $\bar{\alpha} = \alpha_1 - \alpha_2 = J_{jk}(\Delta t_1 - \Delta t_2)$, and vanishes when $\Delta t_1 = \Delta t_2$.

driving the evolution of the system. By cleverly designing a pulse sequence, i.e., a succession of pulses and free evolution periods, one can easily apply two-qubit gates on the state of the system. Indeed, the so-called *refocusing techniques'* principle consists of performing an arbitrary Ising gate by flipping one of the coupled spins (π pulse), as shown in Fig. 3. The interaction evolutions before and after the refocusing pulse compensate leading to the effective evolution

$$U_{j,k}^{\text{eff}} = e^{i(\pi/2)\sigma_x^j} e^{-i(J_{jk}/4)\sigma_z^j \sigma_z^k \Delta t_2} e^{-i\sigma_x^j \pi/2} e^{-i(J_{jk}/4)\sigma_z^j \sigma_z^k \Delta t_1} = e^{-i(\bar{\alpha}/4)\sigma_z^j \sigma_z^k}, \tag{3}$$

where the effective coupling strength $\bar{\alpha} = J_{jk}(\Delta t_1 - \Delta t_2)$ is being determined by the difference between the durations Δt_1 and Δt_2.

We have so far described a quantum register as consisting of nuclei of a single molecule. However, liquid-state NMR uses an ensemble of about 10^{23} molecules in a solution maintained at room temperature ($\simeq 300$ K). For typical values of the magnetic field, this thermal state is extremely mixed. Clearly, this is not the usual state in which we initialize a quantum computation since qubits are nearly randomly mixed. Nevertheless, known NMR methods [16] can be used to prepare the so-called *pseudopure state* (ρ_{pp}) [24]

$$\rho_{pp} = \frac{(1 - \epsilon)}{2^N} I + \epsilon \rho_{\text{pure}}, \tag{4}$$

where ρ_{pure} is a density operator that describes a pure state and ϵ is a small real constant (i.e., ϵ decays exponentially with N).

Under the action of any unitary transformation U this state evolves as

$$\rho_{pp}^{\text{final}} = U \rho_{pp} U^\dagger = \frac{(1 - \epsilon)}{2^N} I + U \epsilon \rho_{\text{pure}} U^\dagger. \tag{5}$$

The first term in Eq. (5) did not change because the identity operator is invariant under any unitary transformation. Therefore performing quantum computation on the ensemble is equivalent to performing quantum computation over the initial state represented only by ρ_{pure}.

At the end of the computation, we measure the orthogonal components of the sample polarization in the *x-y* plane, $M_x = \text{Tr}(\rho_{pp}^{\text{final}}\Sigma_{i=1}^N \sigma_x^i)$, and $M_y = \text{Tr}(\rho_{pp}^{\text{final}}\Sigma_{i=1}^N \sigma_y^i)$. Note that the invariant component of ρ_{pp}^{final} does not contribute to the signal since $\text{Tr}(I\sigma_{x,y}^j) = 0$. Because the polarization of each single spin, $M_x^j = \text{Tr}(\rho_{pp}^{\text{final}}\sigma_x^j)$ and $M_y^j = \text{Tr}(\rho_{pp}^{\text{final}}\sigma_y^j)$, precesses at its own Larmor frequency ν_j, a Fourier transformation of the temporal recording (called FID, for free induction decay) of the total magnetization needs to be performed. By doing so, we obtain the expectation value of the polarization of each spin (averaged over all molecules in the sample).

Summarizing, a liquid-state NMR setting allows us to initialize a register of qubits in a pseudopure state, apply any unitary transformation to this state by sending controlled rf pulses or by free interaction periods, and measure the expectation value of some quantum observables (i.e., the spin polarization). Hence these systems can be used as quantum information processors (QIPs).

III. SIMULATION OF PHYSICAL SYSTEMS

Feynman [6] described a quantum computer as a universal reversible device governed by the laws of quantum physics and capable of exactly simulating any physical system. Although he analyzed the problem of simulating physics assuming that every finite quantum-mechanical system can be imitated exactly by another one (e.g., a set of qubits) [7], he was unsure whether this statement remained valid for the simulation of Fermionic systems.

In this section we describe how to obtain information about physical properties of any quantum many-body system (Fermionic, Bosonic, anyonic, etc.) by using a set of qubits (spin 1/2) controlled by NMR techniques. A more complete description of these methods based on the existence of one-to-one mappings between the algebras used to describe the system to be simulated and the quantum computer [9,11,26], as well as indirect measurement algorithms [8], can be found in previous works [8,10,27].

In this work we are interested in the measurement of correlation functions of the form

$$G(t) = \langle\phi|\hat{U}(t)|\phi\rangle, \tag{6}$$

where $\hat{U}(t)$ is any time (or other continuous parameter)-dependent unitary operator, using indirect measurement techniques [8]. In addition to the qubits used to represent the physical system to be simulated (i.e., the system of qubits), an extra qubit called *ancilla* is required (Fig. 4). This qubit is used as a probe to scan the properties of the system of qubits. It has to be initialized in the superposition state $|+\rangle_{\mathbf{a}} = (|0\rangle_{\mathbf{a}} + |1\rangle_{\mathbf{a}})/\sqrt{2}$ by applying the Hadamard gate [28] to the polarized state $|0\rangle_{\mathbf{a}}$. Then, it interacts with the system of qubits, initially in the state $|\phi\rangle$, through a controlled unitary operation $\mathsf{U}^{|1\rangle_{\mathbf{a}}} = |0\rangle_{\mathbf{a}}\langle 0|\otimes I + |1\rangle_{\mathbf{a}}\langle 1|\otimes\hat{U}(t)$. After this interaction, we can show [8] that $G(t) = \langle 2\sigma_+^{\mathbf{a}}\rangle = \langle\sigma_x^{\mathbf{a}} + i\sigma_y^{\mathbf{a}}\rangle$; that means we get the desired result by measuring the expectation values of the ancilla qubit observables $\sigma_x^{\mathbf{a}}$ and $\sigma_y^{\mathbf{a}}$.

Using the same techniques we can determine the spectrum of an observable $\hat{Q}$ when choosing $\hat{U}(t) = e^{-i\hat{Q}t}$. Figure 5 depicts this algorithm [10]. Since the initial state can always be written as a linear combination of eigenstates of $\hat{Q}$, that is,

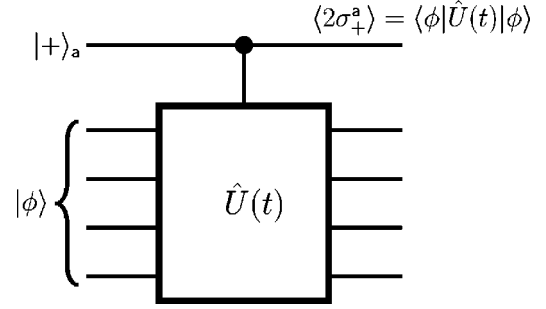$$\langle 2\sigma_+^{\mathbf{a}}\rangle = \langle\phi|\hat{U}(t)|\phi\rangle$$

FIG. 4. Quantum network for the evaluation of the expectation value of a unitary operator $\hat{U}(t)$. The filled circle denotes a controlled operation (i.e., $\mathsf{U}^{|1\rangle_{\mathbf{a}}}$ of Sec. III), such that $\hat{U}(t)$ is applied to the system only if the ancilla qubit is in the state $|1\rangle_{\mathbf{a}}$.

$|\phi\rangle = \Sigma_n\gamma_n|\psi_n\rangle$, with $|\psi_n\rangle$ the eigenstates of $\hat{Q}$ having eigenvalues λ_n, and γ_n complex coefficients, a measurement on the polarization of the ancilla qubit gives $\langle 2\sigma_+^{\mathbf{a}}(t)\rangle = \Sigma_n|\gamma_n|^2 e^{-i\lambda_n t}$. Having the time-dependent function $S(t) = \langle 2\sigma_+^{\mathbf{a}}(t)\rangle$ for a discrete set of values t_i, the eigenvalues λ_n can in principle be obtained by performing a discrete Fourier transform (DFT) [10]. Note that the determination of each single value $S(t_i)$ requires a different experiment.

The eigenvalues λ_n denote the spectrum of a system Hamiltonian H when replacing $\hat{Q} \to H$. In this case, the operation $\mathsf{U}^{|1\rangle_{\mathbf{a}}}$ can be efficiently implemented [8,10,27]. However, methods for finding an initial state with an overlap γ_n that does not vanish exponentially with increasing system size are in general not known. This issue arises, for example, when trying to obtain the spectrum of the two-dimensional Hubbard model approaching the thermodynamic limit [10,27].

Nevertheless, the same basic procedure can be used when interested in obtaining dynamical correlation functions of the form $G(t) = \langle\phi|T^\dagger A_i T B_j|\phi\rangle$ [i.e., $\hat{U}(t) = T^\dagger A_i T B_j$ in Eq. (6)], where $T = e^{-iHt}$ is the time evolution operator of a time-independent Hamiltonian H, and A_i, B_j are unitary operators. In Fig. 6 we show the circuit for an algorithm capable of obtaining these correlation functions after some simplifications [10]. The propagation step is split into three different parts: First, we perform a controlled operation $\mathsf{B}^{|1\rangle_{\mathbf{a}}} = |0\rangle_{\mathbf{a}}\langle 0|\otimes I + |1\rangle_{\mathbf{a}}\langle 1|\otimes B_j$. Second, we perform the T operation on the system, and third, a controlled operation $\mathsf{A}^{|0\rangle_{\mathbf{a}}} = |0\rangle_{\mathbf{a}}\langle 0|\otimes A_i^\dagger + |1\rangle_{\mathbf{a}}\langle 1|\otimes I$. Spatial correlation functions can also be ob-

$$\langle 2\sigma_+^{\mathbf{a}}\rangle = \langle\phi|e^{-i\hat{Q}t}|\phi\rangle$$
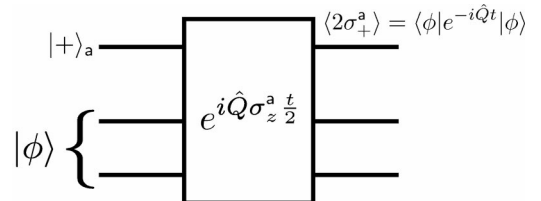
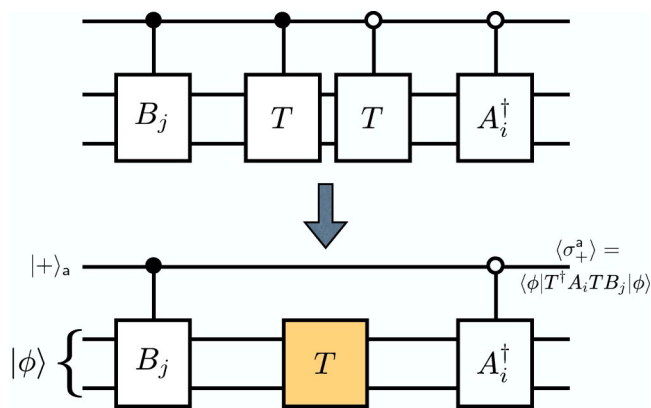FIG. 5. Quantum network for the evaluation of the spectrum of an observable $\hat{Q}$.

FIG. 6. Quantum network for the evaluation of the correlation function $G(t)=\langle\phi|T^\dagger A_i TB_j|\phi\rangle$. The filled (empty) circle denotes an operation controlled by the state $|1\rangle_{\mathbf{a}}(|0\rangle_{\mathbf{a}})$ of the ancilla qubit.
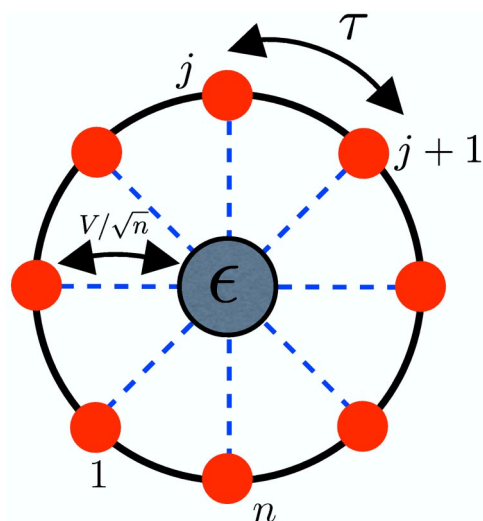

FIG. 7. Fermionic Fano-Anderson model. Fermions can hop between nearest-neighbor sites (exterior circles) and between a site and the impurity (centered circle), with hopping matrix elements τ and $V/\sqrt{n}$, respectively. The energy of a fermion in the impurity is ϵ.

tained when replacing the operator T by the space translation operator. Again, this algorithm can be performed efficiently whenever the initial state $|\phi\rangle$ can be prepared efficiently.

The algorithm described above can be easily implemented with liquid-state NMR methods, since the result of the simulation is encoded in the expectation values of single qubit observables. So far, the algorithm applies only to the simulation of systems described in terms of Pauli operators, such as spin-$1/2$ systems. However, other systems with different particle statistics can also be simulated with these algorithms after mapping their operator algebras onto the Pauli spin-$1/2$ algebra [9,11,26]. In the next section we introduce the Fano-Anderson model, a simple Fermionic system, and show how to simulate it on a liquid-state NMR QIP using these methods.

IV. FANO-ANDERSON MODEL

The quantum simulation of the one-dimensional Fermionic Fano-Anderson model provides a starting point for simulations of quantum systems with different kinds of particle statistics.

The one-dimensional Fermionic Fano-Anderson model consists of an n-sites ring with an impurity in the center (see Fig. 7), where spinless fermions can hop between nearest-neighbors sites with hopping matrix element (overlap integral) τ, or between a site and the impurity with matrix element $V/\sqrt{n}$. Taking the single-particle energy of a fermion in the impurity to be ϵ, and considering the translational invariance of the system, the Fano-Anderson Hamiltonian can be written in the wave-vector representation as [8]

$$H = \sum_{l=0}^{n-1} \varepsilon_{k_l} c^\dagger_{k_l} c_{k_l} + \epsilon b^\dagger b + V(c^\dagger_{k_0} b + b^\dagger c_{k_0}), \quad (7)$$

where the Fermionic operators $c^\dagger_{k_l}$ and $b^\dagger$ (c_{k_l} and b) create (destroy) a spinless fermion in the conduction mode k_l and in the impurity, respectively. Here, the wave vectors are $k_l = 2\pi l/n (l=[0,\ldots,n-1])$ and the energies per mode are $\varepsilon_{k_l} = -2\tau \cos k_l$.

In this form, the Hamiltonian in Eq. (7) is almost diagonal and can be exactly solved: There are no interactions between

electrons in different modes k_l, except for the mode k_0, which interacts with the impurity. Therefore the relevant physics comes from this latter interaction, and its spectrum can be exactly obtained by diagonalizing a 2×2 Hermitian matrix, regardless of n and the number of fermions in the ring N_e. Nevertheless, its simulation in a liquid-state NMR QIP is the first step in quantum simulations of quantum many-body problems.

In order to use the algorithms presented in Sec. III, and to successfully simulate this system in an NMR QIP, we first need to map the Fermionic operators onto the spin-$1/2$ (Pauli) operators. This is done by use of the following Jordan-Wigner transformation [26]:

$$b = \sigma^1_- \qquad\qquad b^\dagger = \sigma^1_+$$

$$c_{k_0} = -\sigma^1_z\sigma^2_- \qquad c^\dagger_{k_0} = -\sigma^1_z\sigma^2_+$$

$$\vdots \qquad\qquad\qquad \vdots \qquad\qquad (8)$$

$$c_{k_{n-1}} = (\prod_{j=1}^{n} -\sigma^j_z)\sigma^{n+1}_- \quad c^\dagger_{k_{n-1}} = (\prod_{j=1}^{n} -\sigma^j_z)\sigma^{n+1}_+.$$

In this language, a logical state $|0_j\rangle$ (with $|0\rangle\equiv|\uparrow\rangle$ in the usual spin-$1/2$ notation) corresponds to having a spinless fermion in either the impurity, if $j=1$, or in the mode k_{j-2}, otherwise. The Fermionic vacuum state $|\mathsf{vac}\rangle$ (i.e., the state with no fermions) maps onto $|\widehat{\mathsf{vac}}\rangle=|1_1 1_2\cdots 1_{n+1}\rangle$ $(\equiv|\downarrow_1\downarrow_2\cdots\downarrow_{n+1}\rangle)$. As an example, Fig. 8 shows the mapping of a particular Fermionic state for $n=4$.

Some dynamical properties of this model can be obtained using the quantum algorithms described in Sec. III. Here, we are primarily interested in obtaining the probability amplitude of having a fermion in mode k_0 at time t, if initially ($t=0$) the quantum state is the Fermi sea state with N_e fermions; that is, $|\mathsf{FS}\rangle=\Pi_{l=0}^{N_e-1}c^\dagger_{k_l}|\mathsf{vac}\rangle$. This probability is given by

FIG. 9. Quantum circuit for the evaluation of $G(t)$ [Eq. (9)] in terms of elementary gates directly implementable with liquid-state NMR methods.

$$G(t) = \langle\phi|e^{i\bar{H}t}\sigma_x^1 e^{-i\bar{H}t}\sigma_x^1|\phi\rangle. \tag{12}$$

Figure 9 shows the quantum circuit used to obtain $G(t)$. It is derived from Fig. 6 by making the following identifications: $T \rightarrow e^{-i\bar{H}t}$, $A_i \rightarrow \sigma_x^1$, and $B_j \rightarrow \sigma_x^1$. As we can see, the corresponding controlled operations $\mathsf{A}^{|0\rangle_\mathbf{a}}$ and $\mathsf{B}^{|1\rangle_\mathbf{a}}$ (Sec. III) transform into the well-known controlled-not (CNOT) gates. All the unitary operations appearing in Fig. 9 were decomposed into elementary NMR gates (single qubit rotations and Ising interactions). In particular, the decomposition of $e^{-i\bar{H}t}$ can be found in Ref. [8]. We obtain

$$e^{-i\bar{H}t} = U e^{-i\lambda_1 \sigma_z^1 t} e^{-i\lambda_2 \sigma_z^2 t} U^\dagger, \tag{13}$$

where $\lambda_{1(2)} = \frac{1}{2}(E \mp \sqrt{\Delta^2 + V^2})$, with $E = (\epsilon + \varepsilon_{k_0})/2$, and $\Delta = (\epsilon - \varepsilon_{k_0})/2$. The unitary operator U is decomposed as (Fig. 9)

$$U = e^{i(\pi/4)\sigma_x^2} e^{-i(\pi/4)\sigma_y^1} e^{-i(\theta/2)\sigma_z^1 \sigma_z^2} e^{i(\pi/4)\sigma_y^1} e^{i(\pi/4)\sigma_x^1} e^{-i(\pi/4)\sigma_x^2}$$
$$\times e^{-i(\pi/4)\sigma_y^2} e^{i(\theta/2)\sigma_z^1 \sigma_z^2} e^{-i(\pi/4)\sigma_x^1} e^{i(\pi/4)\sigma_y^2}, \tag{14}$$

with the parameter θ satisfying $\cos\theta = 1/\sqrt{1+\delta^2}$, and $\delta = (\Delta + \sqrt{\Delta^2 + V^2})/V$.

The CNOT gates $\mathsf{A}^{|0\rangle_\mathbf{a}}$ and $\mathsf{B}^{|1\rangle_\mathbf{a}}$ can also be decomposed into elementary gates, obtaining

$$\mathsf{A}^{|0\rangle_\mathbf{a}} = |0\rangle_\mathbf{a}\langle 0| \otimes \sigma_x^1 + |1\rangle_\mathbf{a}\langle 1| \otimes I$$
$$= e^{i(\pi/4)\sigma_x^1} e^{i(\pi/4)\sigma_z^1 \sigma_z^\mathbf{a}} e^{-i(\pi/4)\sigma_y^1} e^{-i(\pi/4)\sigma_z^1 \sigma_z^\mathbf{a}} e^{-i(\pi/4)\sigma_z^1}$$

and

$$\mathsf{B}^{|1\rangle_\mathbf{a}} = |0\rangle_\mathbf{a}\langle 0| \otimes I + |1\rangle_\mathbf{a}\langle 1| \otimes \sigma_x^1$$
$$= e^{i(\pi/4)\sigma_x^1} e^{-i(\pi/4)\sigma_z^1 \sigma_z^\mathbf{a}} e^{-i(\pi/4)\sigma_y^1} e^{i(\pi/4)\sigma_z^1 \sigma_z^\mathbf{a}} e^{-i(\pi/4)\sigma_z^1}$$

(up to a phase factor). Therefore we can implement the circuit of Fig. 9 and obtain $G(t)$ using an NMR QIP by applying the appropriate rf pulses (Sec. II). Only three qubits are required for its simulation (Fig. 9): The ancilla qubit **a**, one qubit representing the impurity site (qubit 1), and one qubit representing the k_0 mode (qubit 2).

$$b^\dagger c_{k_0}^\dagger c_{k_2}^\dagger |\mathsf{vac}\rangle \leftrightarrow |\uparrow_1 \uparrow_2 \downarrow_3 \uparrow_4 \downarrow_5\rangle \leftrightarrow |0_1 0_2 1_3 0_4 1_5\rangle$$
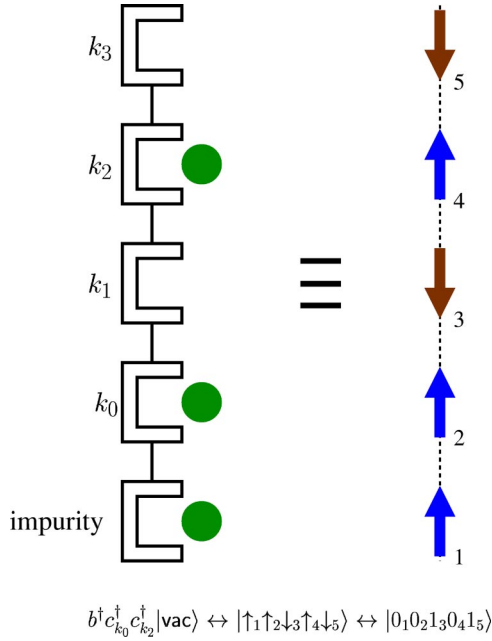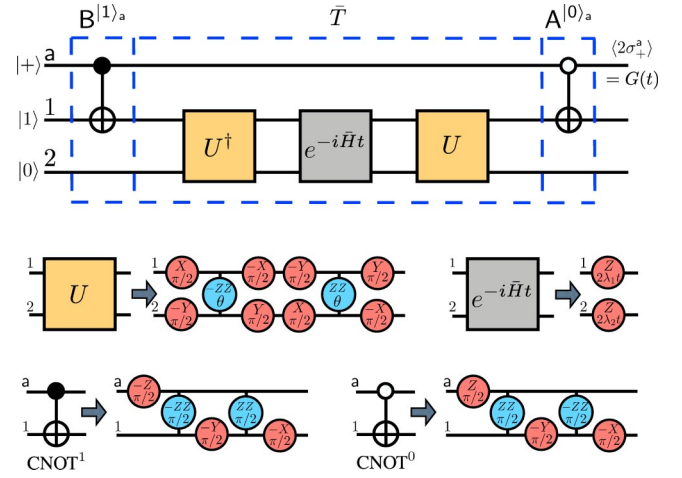
FIG. 8. Mapping of the Fermionic product state $c_1^\dagger c_2^\dagger c_4^\dagger|\mathsf{vac}\rangle$, with $|\mathsf{vac}\rangle$ the no-fermion or vacuum state, into the spin-1/2 and the standard quantum computation languages, using the Jordan-Wigner transformation. A filled circle denotes a site occupied by a spinless fermion, which maps into the state $|\uparrow\rangle$ in the spin-1/2 algebra.

the modulus square of the following dynamical correlation function:

$$G(t) = \langle\mathsf{FS}|b(t)b^\dagger(0)|\mathsf{FS}\rangle, \tag{9}$$

where $b(t) = T^\dagger b(0) T$, $T = e^{-iHt}$ is the time evolution operator, and $b^\dagger(0) = b^\dagger$. Basically, $G(t)$ is the overlap between the quantum state $b^\dagger(0)|\mathsf{FS}\rangle$, which does not evolve, and the state $b^\dagger(t)|\mathsf{FS}\rangle$, which does not vanish unless the evolved state $T|\mathsf{FS}\rangle$ already contains a fermion in the impurity site ($[b^\dagger(t)]^2 = [b^\dagger(0)]^2 = 0$), i.e., contains the fermion which initially was in the k_0 mode. In terms of spin-1/2 operators [see Eq. (8)], this correlation function reduces to a two-qubit problem [8]:

$$G(t) = \langle\phi|\bar{T}^\dagger \sigma_-^1 \bar{T} \sigma_+^1|\phi\rangle, \tag{10}$$

where $\bar{T} = e^{-i\bar{H}t}$ is an evolution operator arising from the interaction terms in Eq. (7), with

$$\bar{H} = \frac{\epsilon}{2}\sigma_z^1 + \frac{\varepsilon_{k_0}}{2}\sigma_z^2 + \frac{V}{2}(\sigma_x^1\sigma_x^2 + \sigma_y^1\sigma_y^2), \tag{11}$$

and $|\phi\rangle = |1_1 0_2\rangle$ in the logical basis (i.e., the initial state with one fermion in the k_0 mode).

In order to use the quantum circuit shown in Fig. 6, all operators in Eq. (10) must be unitary. Using the symmetries of H, such as the global $\pi/2$ z rotation that maps $(\sigma_x^j, \sigma_y^j) \rightarrow (\sigma_y^j, -\sigma_x^j)$, leaving the state $|\phi\rangle$ invariant (up to a phase factor), we obtain $\langle\phi|\bar{T}^\dagger \sigma_x^1 \bar{T}\sigma_y^1|\phi\rangle = \langle\phi|\bar{T}^\dagger \sigma_y^1 \bar{T}\sigma_x^1|\phi\rangle = 0$ and $\langle\phi|\bar{T}^\dagger \sigma_x^1 \bar{T}\sigma_x^1|\phi\rangle = \langle\phi|\bar{T}^\dagger \sigma_y^1 \bar{T}\sigma_y^1|\phi\rangle$. Then, Eq. (10) can be written in terms of unitary operators as
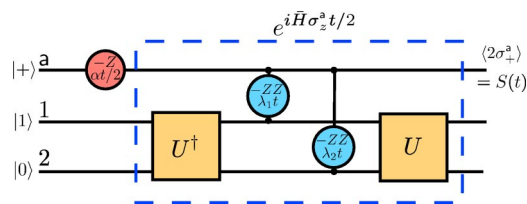
FIG. 10. Quantum circuit for the evaluation of $S(t)$ [Eq. (15)]. The parameters λ_1 and λ_2 are defined in Sec. IV, and $\alpha=(\epsilon+\varepsilon_{k_0})/2$. The decomposition of the operator U in NMR gates can be found in Fig. 9.

FIG. 11. The transcrotonic acid molecule is a seven-qubit register: Two protons, the methyl group used as a single spin-1/2 [29] and four ^{13}C. The table shows in hertz the values of the chemical shifts (on the main diagonal) and the J couplings (off-diagonal) between every pair of nuclei (qubits).

	C_1	C_2	C_3	C_4	M	H_1	H_2
C_1	−1914.06	40.5	1.5	7	127	3.9	6.3
C_2		−18115.10	69.9	1.3	−7.1	155.1	−0.6
C_3			−15157.41	73.2	6.6	−1.8	163
C_4				−21148.90	−0.9	6.5	3.6
M					230.43	6.9	−1.7
H_1						−2370.80	15.5
H_2							−1774.47

We are also interested in obtaining the spectrum of the Hamiltonian H of Eq. (7). For this purpose we used the algorithm shown in Fig. 5, replacing $\hat{Q} \rightarrow H$. In particular, when $n=1$ (one site plus the impurity), Eq. (7) reduces to $H=(\epsilon+\varepsilon_{k_0})/2+\bar{H}$, with $\bar{H}$ defined in Eq. (11) in terms of Pauli operators. In this case, the two eigenvalues $\lambda_i(i=1,2)$ of the one-particle subspace can be extracted from the correlation function (Sec. III)

$$S(t) = \langle\phi|e^{-iHt}|\phi\rangle = e^{-i(\epsilon+\varepsilon_{k_0})t}\langle\phi|e^{-i\bar{H}t}|\phi\rangle, \quad (15)$$

which can be obtained by measuring the polarization of the ancilla qubit after the quantum circuit shown in Fig. 5 has been applied. Since $|\phi\rangle=|1_1 0_2\rangle=|\downarrow_1\uparrow_2\rangle$ is not an eigenstate of H, it has a nonzero overlap with the two one-particle eigenstates, called $|1P_i\rangle$ (see the Appendix).

Again, the operator $e^{iH\sigma_z^{\mathbf{a}}t/2}$ (Fig. 5) needs to be decomposed into elementary gates for its implementation in an NMR QIP. Noticing that $[\sigma_z^{\mathbf{a}},H]=[\sigma_z^{\mathbf{a}},U]=0$, we obtain

$$e^{iH\sigma_z^{\mathbf{a}}t/2} = Ue^{i\lambda_1\sigma_z^1\sigma_z^{\mathbf{a}}t/2}e^{i\lambda_2\sigma_z^2\sigma_z^{\mathbf{a}}t/2}U^{\dagger}e^{i(\epsilon+\varepsilon_{k_0})\sigma_z^{\mathbf{a}}t/2}, \quad (16)$$

where the unitary operator U is decomposed as in Eq. (14). Figure 10 shows the corresponding circuit in terms of elementary gates. Again, qubits 1 and 2 represent the impurity site and the k_0 mode, respectively. **a** denotes the ancilla qubit. Since the idea is to perform a DFT on the results obtained from the measurement (see the Appendix), we need to apply this circuit for several values of the parameter t (Sec. III).

V. EXPERIMENTAL IMPLEMENTATION

A. Experimental protocol

For the experimental simulation of the Fermionic Fano-Anderson model, we used an NMR QIP based on a solution of transcrotonic acid and methanol dissolved in acetone. This setting has been described in Ref. [29]. Once the state of the three equivalent protons in the methyl group of the transcrotonic acid molecule is projected onto the spin-1/2 subspace [29], this molecule can be used as a seven-qubit register (see Fig. 11). Methanol is used to perform rf-power selection and accurately calibrate the rf pulses.

Two important characteristics of a molecule used for an NMR QIP are: (i) the accuracy of the control and (ii) the number of elementary gates we can perform within the rel-

evant decoherence time of the system. The accuracy of control in transcrotonic acid has been determined in Ref. [30], using an error-correcting code as a benchmark. The current experiment can be considered as another exploration of the accuracy of control, in this case examining how well we can implement the necessary evolutions when simulating quantum systems with NMR techniques.

In liquid-state NMR the main source of decoherence is the relaxation of the transversal polarization of the sample due to the loss of coherence between molecules. In our setting, the relevant times of this process, called T_2^*, are in the range from several hundreds of milliseconds to more than one second, for the different nuclei. These times fix the maximum number of elementary gates that can be applied to the quantum register without losing coherence. Indeed, a lower bound of the pulse duration to induce a rotation on a single qubit is determined by the difference between the resonant frequencies of the spin to be rotated and the others (its chemical shift). A very short pulse having a wide excitation profile in the frequency domain affects several spins at the same time if their chemical shifts are small. On the other hand, the duration of the Ising gate (two-qubit gate) depends directly on the strength of the J-coupling constants J_{jk}. In our setting the chemical shifts values impose pulse durations of the order of 1 ms, and the J couplings impose interaction periods of the order of 10 ms, restricting the pulse sequences to a maximum of approximately 1000 single-qubit rotations and 100 two-qubit (Ising) gates.

Designing a pulse sequence to implement exactly the desired unitary transformation would require very long refocusing schemes to cancel out all the unwanted naturally occurring J couplings. Then, the overall duration of the pulse sequence increases and decoherence effects could destroy our signal. Therefore we need to find the best tradeoff between the ideal [31] accuracy of the pulse sequence and its duration, and neglect small couplings. For this purpose, we used an efficient pulse sequence compiler to perform the phase tracking calculations and to numerically optimize the delays between pulses, in order to minimize the error that we introduce into the quantum computation by neglecting small couplings.

We now describe the parts of the pulse sequence corresponding to the basic steps of the quantum simulation.

1. Pseudopure state preparation

Initially, the state of the nuclei of the transcrotonic acid molecules in solution is given by the thermal distribution
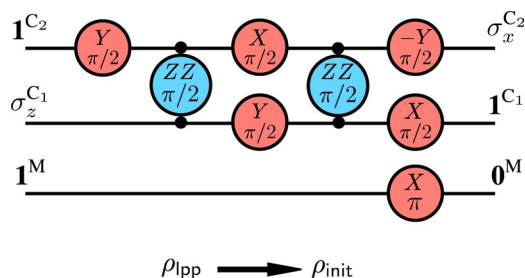
FIG. 12. Initialization pulse sequence used to transform the initial labeled pseudopure state $\rho_{lpp}=\mathbf{1}^{C_2}\sigma_z^{C_1}\mathbf{1}^M$ into the state $\rho_{init}=\sigma_x^{C_2}\mathbf{1}^{C_1}\mathbf{0}^M$. The sequence transfers the polarization from C_1 to C_2 and flips the spin of the methyl group M. We have chosen the spin-$1/2$ nuclei C_2, C_1, and M to represent the ancilla, qubit 1 (i.e., the impurity), and qubit 2 (i.e., the k_0 mode), respectively.

(Sec. II). Using the methods described in Ref. [29] we have prepared the labeled pseudopure state (lpp) $\rho_{lpp}=\mathbf{1}^{C_4}\mathbf{1}^{C_3}\mathbf{1}^{C_2}\sigma_z^{C_1}\mathbf{1}^M\mathbf{1}^{H_2}\mathbf{1}^{H_1}$, where $\mathbf{1}=\frac{1}{2}[I-\sigma_z]$ (i.e., $\mathbf{1}=|1\rangle\langle1|$) and $\mathbf{0}=\frac{1}{2}[I+\sigma_z]$ (i.e., $\mathbf{0}=|0\rangle\langle0|$). As we will see, the state ρ_{lpp}, having the spin of C_1 in the σ_z state, is a good initial state for our purposes.

2. Initialization

As mentioned in Sec. IV, we need only three qubits to simulate the Fano-Anderson model. These qubits must be well coupled to each other to decrease the duration of the corresponding Ising gates we apply to them. We have chosen the spin-$1/2$ nucleus C_1 to represent qubit 1 (i.e., the impurity) and the spin-$1/2$ nucleus M to represent qubit 2 (i.e., the k_0 mode). On the other hand, we have chosen the spin-$1/2$ nucleus C_2 to be the ancilla qubit **a**, to take advantage of its strong coupling with the spin-$1/2$ nucleus C_1 (qubit 1). Since the rest of the spins (C_4, C_3, H_2, H_1) in the molecule remain in the state **1** or **0** during the whole duration of the experiment, we need to consider only the spins $C_2 \otimes C_1 \otimes M$ with the above identification [32].

The initial state $|+\rangle_\mathbf{a} \otimes |1_1 0_2\rangle$ (Sec. IV) can be written as $\rho'_{init}=\frac{1}{2}[(I^\mathbf{a}+\sigma_x^\mathbf{a})\mathbf{1}^1\mathbf{0}^2]$ in terms of Pauli operators. The ancilla qubit is only a *control qubit* and its state (i.e., its reduced density matrix) becomes correlated with the rest of the qubits. Moreover, considering that the identity part is not observable, we used $\rho_{init}=\sigma_x^\mathbf{a}\mathbf{1}^1\mathbf{0}^2$ instead of ρ'_{init} as the initial state. Its preparation was done by applying a sequence of elementary gates to $\rho_{lpp}=\mathbf{1}^\mathbf{a}\sigma_z^1\mathbf{1}^2$, as shown in Fig. 12.

3. Propagation pulse sequence

As shown in Fig. 10, the pulse sequence used for obtaining $S(t)$ [Eq. (15)] requires Ising gates with a coupling strength depending on t. The refocusing schemes are then optimized differently and the results for different values of t cannot be directly comparable. To avoid this problem we have replaced the two Ising gates by an equivalent sequence of elementary gates, where the dependence on the simulation parameter t is transferred into the angle of a single-qubit rotation around the z axis (Fig. 13). This *virtual* rotation is implemented through a phase tracking, as mentioned in Sec.
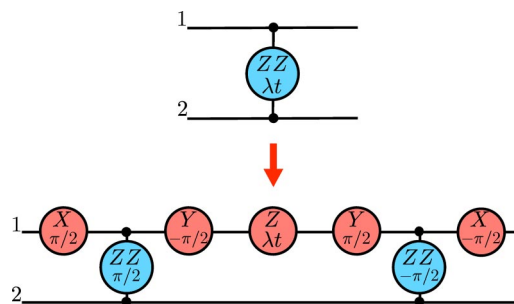

FIG. 13. Modification of a two-qubit gate with a coupling strength depending on a parameter t. The variable interaction period is translated into fixed interaction periods and a single-qubit rotation with variable angle about the z axis. Using this modified gate, the refocusing schemes of the pulse sequences do not depend on the parameter t.

II. Thus the only difference between the pulse sequence used to measure $S(t)$ for different simulation times t_i is a phase calculation that introduces no extra optimization or experimental error.

4. Measurement

The result of the algorithm is encoded in the polarization of the ancilla qubit $\langle 2\sigma_+^\mathbf{a}\rangle=\langle\sigma_x^\mathbf{a}\rangle+i\langle\sigma_y^\mathbf{a}\rangle$ (Sec. III), which is directly proportional to the polarization of C_2 over the sample. This component precesses at the C_2 Larmor frequency ν_{C_2}. To measure it, we have to perform a Fourier transformation on the measured FID and integrate only the peak located at ν_{C_2}. Nevertheless, the absolute value of this signal is irrelevant since it depends on many experimental parameters such as the solution concentration, the probe sensitivity, and the gain of the amplifier. The relevant quantity is its intensity relative to a reference signal given by the observation of the initial state ρ_{init}. To get a good signal-to-noise ratio, each experiment (or *scan*) was done several times and the corresponding experimental data were added.

Moreover, to average over small magnetic fluctuations occurring within the duration of the whole experiment we interlaced scans of the reference experiment (i.e., the measurement of the reference signal) with scans of the actual complete pulse sequence. To increase the spatial homogeneity of the field over the sample we also have inserted several automated shimming periods consisting of fine tuning of small additional coils located around the sample.

B. Results

1. Correlation function

In the first experiment we measured the correlation function $G(t)$ [Eq. (9)] for two different sets of parameters in the Hamiltonian of Eq. (7): $\varepsilon_{k_0}=-2$, $\epsilon=-8$, $V=4$, varying t from 0.1 to 1.5 s using increments of $\Delta t=0.1$ s, and $\varepsilon_{k_0}=-2$, $\epsilon=0$, $V=4$, varying t from 0.1 to 3.1 s with $\Delta t=0.1$ s. The duration of the optimized pulse sequences from the beginning of the initialization step to the beginning of the data acquisition, was 97 ms. In Fig. 14 we show the analytical
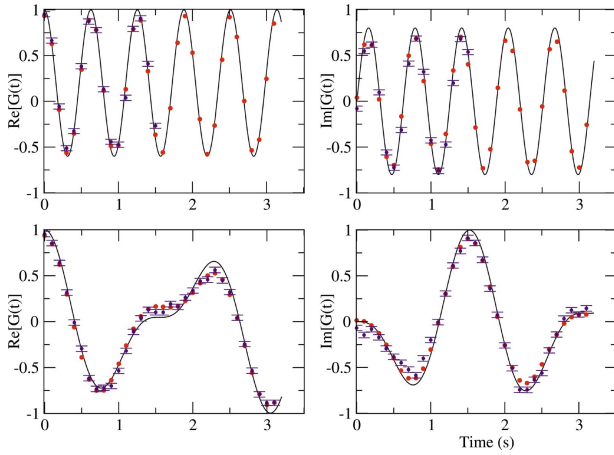
FIG. 14. (Color) Real and imaginary parts of the correlation function $G(t)$ of Eq. (9). The top panels show the results when the parameters in Eq. (7) are $\varepsilon_{k_0}=-2$, $\epsilon=-8$, $V=4$. The corresponding parameters $\lambda_1, \lambda_2, \theta$ used in the quantum network (Fig. 9) can be determined using Eqs. (13) and (14). The bottom panels show the results for $\varepsilon_{k_0}=-2$, $\epsilon=0$, $V=4$. The (black) solid line is the analytic solution, the red circles are obtained by the numerical simulation (including the refocusing pulses), and the blue circles with the error bars are experimental data.

form of $G(t)$ [8], as well as the simulated and experimental data points. The simulated data points were obtained by a numerical simulation of the Hamiltonian dynamics of the full seven-qubit register under the optimized pulse sequence. This simulation is of course inefficient but still tractable on a conventional desktop computer.

2. Hamiltonian spectrum

In the second experiment we measured the function $S(t)$ of Eq. (15) to determine the eigenvalues of Eq. (7), for $\varepsilon_{k_0}=-2$, $\epsilon=-8$, and $V=0.5$. The pulse sequence applied is the one corresponding to the quantum circuit shown in Fig. 10 with the corresponding refocusing pulses. Its duration was about 65 ms. We have repeated this experiment for 128 different values of the parameter t [Eq. (15)], from $t=0.1$ to 12.8 s, using increments of $\Delta t=0.1$ s.

In Fig. 15 we show the analytical, numerically simulated, and experimental results for the evaluation of $S(t)$. As mentioned in Sec. III, a DFT needs to be performed in order to extract the corresponding eigenvalues. In Fig. 16 we show the DFT of the experimental data (see the Appendix), which reveals the expected peaks at the frequency of the two eigenvalues of Eq. (7) in the one-particle sector, for the above parameters.

C. Discussion

At the experimental points, the error bars depend directly on the signal-to-noise ratio of our experimental data, as it is obtained after a fit to the experimental measured FID. They can then be reduced simply by running more scans for each experiment. All presented results have been obtained after eight scans.
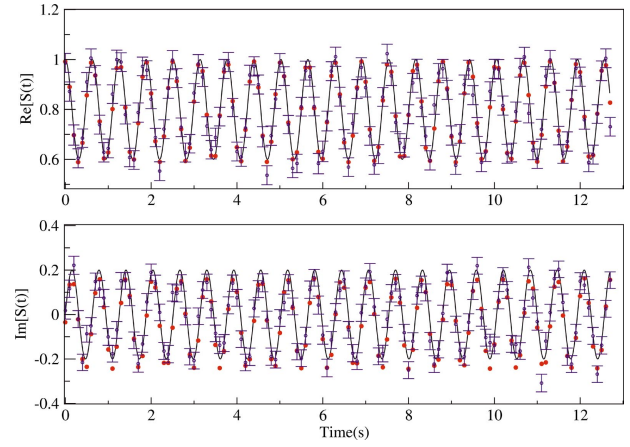

FIG. 15. (Color) Real and imaginary parts of $S(t)$, for $\varepsilon_{k_0}=-2$, $\epsilon=-8$, and $V=0.5$ in Eq. (7). The (black) solid line corresponds to the analytic solution. The red circles correspond to the numerical simulation (using refocusing pulses) and the blue circles with the error bars are experimental data. $S(t)$ has been measured using the network of Fig. 10 with $\alpha=(\epsilon+\varepsilon_{k_0})/2$.

Two different classes of errors affect the accuracy of the experimental results. The first, *purely experimental*, type of error is due to the finite accuracy of the spectrometer, and the intrinsic decoherence of the physical system we are working with. The second type of error is due to the incomplete refocusing induced by the numerical optimization scheme we used to design the pulse sequence. The numerical simulation of the optimized pulse sequence includes the errors of the second class but does not take into account the purely experimental ones. Thus, in our case, the good agreement between experimental results and simulations suggests that the main contribution to errors comes from the incomplete refocusing in the optimization procedure. Increasing the number of refocusing pulses might have led to more accurate results even if they would have increased the overall duration of the pulse sequences. The good agreement between experiment and simulation is consistent with the fact that the current duration of the pulse sequences are much smaller than the relevant relaxation time of the system (T_2^*).
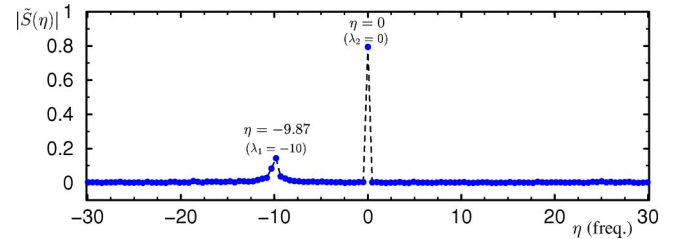

FIG. 16. Discrete Fourier transform of the real part of the experimental data of Fig. 15. The position of the two peaks corresponds to the two eigenvalues of the Hamiltonian of Eq. (7) for $\varepsilon_{k_0}=-2$, $\epsilon=-8$, and $V=0.5$. Numbers in parentheses denote the exact solution. The size of the dots representing experimental points is the error bar (see the Appendix). An upper bound to the error in the frequency domain is ≈ 0.5, which was determined by the resolution of the spectrum due to the time sampling of the simulation (Sec. V B).

VI. CONCLUSIONS

We have successfully simulated a quantum many-fermion system using a liquid-state NMR based QIP. The algebraic mapping of the operators describing *any* anyonic system onto the Pauli operators describing our QIP, combined with indirect measurement techniques, allow us to design efficient algorithms to simulate arbitrary evolutions of many-body anyonic systems.

In this work the system studied was the Fermionic Fano-Anderson model, which can be mapped onto a two-qubit system by use of the standard Jordan-Wigner transformation. Relevant dynamical correlation functions of the form $G(t) = \langle \phi | T^\dagger A_i T B_j | \phi \rangle$ can be obtained by executing quantum algorithms based on indirect quantum measurements, i.e., using an additional ancilla qubit. Then, the algorithms needed to simulate this particular system require three qubits, regardless of the number of sites n (Fig. 7). We were able to design and run pulse sequences to implement these algorithms on an NMR QIP based on the transcrotonic acid molecule (a seven-qubit quantum register). The results obtained agree with the theoretical ones. To keep a constant error level, each pulse sequence has been transformed such that the time parameters t_i enter as a phase dependence. To shorten the duration of the pulse sequence and decrease the effect of decoherence we used only an approximate refocusing scheme. We numerically optimized these pulse sequences to minimize the errors of the quantum simulation. These techniques allowed us to get very accurate results with efficiently controlled errors, since the overall duration of the pulse sequence was much smaller than the decoherence time of the system.

Although the addition of particle-particle (e.g., density-density or exchange) interactions in the Fano-Anderson Hamiltonian makes it, in general, nonintegrable, the quantum simulation of $G(t)$ remains efficient, i.e., with polynomial complexity. The simulation of these more realistic systems would still require bigger registers and longer pulse sequences, and therefore it would suffer from an increase of systematic errors as well as decoherence effects. Nevertheless, quantum error correction and fault-tolerant procedures provide, in principle, an efficient way to overcome this potential problem [33,34]. We can therefore conclude that this work constitutes an experimental proof of principle for efficient methods to simulate quantum many-body systems with quantum computers.

APPENDIX: DISCRETE FOURIER TRANSFORM AND PROPAGATION OF ERRORS

Theoretically, the function $S(t)$ of Eq. (15) is a linear combination of two complex functions having different frequen-

cies: $S(t) = |\gamma_1|^2 e^{-i\lambda_1 t} + |\gamma_2|^2 e^{-i\lambda_2 t}$, where λ_i are the eigenvalues of the one-particle eigenstates, defined as $|1P_i\rangle$, in the Fano-Anderson model with $n=1$ site and the impurity (see Sec. IV), and $\lambda_i = |\langle \phi | 1P_i \rangle|^2$ (Sec. III), with $|\phi\rangle = |\downarrow_1 \uparrow_2 \rangle$ [8]. However, the liquid NMR setting used to measure $S(t)$ experimentally adds a set of errors that cannot be controlled, and the function $S(t)$ shown in Fig. 15 is no longer a contribution of two different frequencies only.

As mentioned in Sec. V B, $S(t)$ was obtained experimentally for a discrete set of values $t_j = j\Delta t$, with $j = [1, \ldots, M = 128]$ and $\Delta t = 0.1$ s. Its DFT is given by

$$\widetilde{S}(\eta_l) = \frac{1}{M} \sum_{j=1}^{M} S(t_j) e^{i \eta_l t_j}, \tag{A1}$$

where $S(t_j)$ is the experimental value of $S(t)$ at time t_j, and $\eta_l = 2\pi l / M\Delta t$ (with $l = [1, \ldots, M]$) are the discrete set of frequencies that contribute to $S(t)$ [35]. Notice that since we are evaluating the spectrum of a physical (Hermitian) Hamiltonian, the imaginary part of $\widetilde{S}(\eta_l)$ is zero [36]. In Fig. 16 we show $\widetilde{S}(\eta_l)$ obtained from the experimental points $S(t_j)$ of Fig. 15. Its error bars (i.e., the size of the line in the figure) were calculated by considering the experimental error bars of $S(t_j)$ in the following way: First, we rewrite Eq. (A1) as

$$\widetilde{S}(\eta_l) = \sum_{j=1}^{M} Q_{lj}, \tag{A2}$$

with $Q_{lj} = M^{-1}\{\text{Re}[S(t_j)]\cos(\eta_l t_j) - \text{Im}[S(t_j)]\sin(\eta_l t_j)\}$ (real). Then, the approximate standard deviation $\mathsf{E}\widetilde{S}_l$ of $\widetilde{S}(\eta_l)$ depends on the errors $\mathsf{E}Q_{lj}$ of Q_{lj} as (considering a normal distribution [37])

$$[\mathsf{E}\widetilde{S}_l]^2 \approx \sum_{j=1}^{M} [\mathsf{E}Q_{lj}]^2. \tag{A3}$$

On the other hand, $\mathsf{E}Q_{lj}$ is calculated as [37]

$$[\mathsf{E}Q_{lj}]^2 = \left| \frac{\partial Q_{lj}}{\partial \, \text{Re}[S(t_j)]} \right|^2 \mathsf{E}_\mathsf{R}^2 + \left| \frac{\partial Q_{lj}}{\partial \, \text{Im}[S(t_j)]} \right|^2 \mathsf{E}_\mathsf{I}^2, \tag{A4}$$

where E_R and E_I are the standard deviations of the real and imaginary parts of $S(t_j)$ (see Fig. 15), respectively. Because of experimental reasons (Sec. V A) these errors are almost constant, having $\mathsf{E}_\mathsf{R} \sim \mathsf{E}_\mathsf{I} \sim \mathsf{E}_\mathsf{S}$ independently of t_j (see Fig. 15), where E_S is taken as the largest standard deviation. Combining Eqs. (A3) and (A4), we obtain

$$\mathsf{E}\widetilde{S}_l = \left[M^{-2} \mathsf{E}_\mathsf{S}^2 \sum_{j=1}^{M} \left[|\cos(\eta_l t_j)|^2 + |\sin(\eta_l t_j)|^2 \right] \right]^{1/2} = \frac{\mathsf{E}_\mathsf{S}}{\sqrt{M}}. \tag{A5}$$

In our experiment, $M = 128$ and $\mathsf{E}_S \approx 0.04$, obtaining $\mathsf{E}\widetilde{S}_l \approx 0.0035$, which determines the (constant) error bars (i.e., the size of the dots representing data points) shown in Fig. 16.

The standard deviation $\mathsf{E}\,\eta_l$ in frequency domain is due to the resolution of the sampling time Δt. This resolution is related to the error coming from the implementation of the z rotations in the refocusing procedure (Fig. 3). A bound for this error is given by the resolution of the spectrum; that is,

$$\mathsf{E}\,\eta_l \leqslant \frac{2\pi}{M\Delta t} \approx 0.5. \qquad (A6)$$

[1] P. Shor, *Proceedings of the 35th Annual IEEE Symposium on Foundations of Computer Science*, FOCS'94, Santa Fe, New Mexico 1994, pp. 124–134.

[2] L. K. Grover, *Proceedings of the 28th Annual ACM Symposium on Theory of Computing* (STOC), New York, 1996, pp. 212–219.

[3] A. Ambainis, quant-ph/0311001.

[4] A. Kitaev, quant-ph/9511026.

[5] M. Mosca and A. Ekert, quant-ph/9903071.

[6] R. P. Feynman, Int. J. Theor. Phys. **21**, 467 (1982).

[7] In Feynman's words, "If you had discrete quantum systems, what other discrete quantum systems are exact imitations of it, and is there a class against which everything can be matched? I believe it's rather simple to answer that question and to find the class, but I just haven't done it."

[8] G. Ortiz, J. Gubernatis, E. Knill, and R. Laflamme, Phys. Rev. A **65**, 042323 (2001).

[9] C. D. Batista and G. Ortiz, Phys. Rev. Lett. **86**, 1082 (2001).

[10] R. Somma, G. Ortiz, J. E. Gubernatis, E. Knill, and R. Laflamme, Phys. Rev. A **65**, 022319 (2002).

[11] C. D. Batista and G. Ortiz, Adv. Phys. **53**, 1 (2004).

[12] S. Lloyd, Science **273**, 1073 (1996).

[13] For example, H. Q. Lin and J. E. Gubernatis, Comput. Phys. **7**, 400 (1993).

[14] D. M. Ceperley, Rev. Mod. Phys. **67**, 279 (1995).

[15] For example, B. B. Beard and U.-J. Wiese, Phys. Rev. Lett. **77**, 5130 (1996).

[16] R. Laflamme, E. Knill, D. G. Cory, E. M. Fortunato, T. Havel, C. Miquel, R. Martinez, C. Negrevergne, G. Ortiz, M. A. Pravia, Y. Sharf, S. Sinha, R. Somma, and L. Viola, Los Alamos Sci. **27**, 226 (2002).

[17] C. H. Tseng, S. Somaroo, Y. Sharf, E. Knill, R. Laflamme, T. F. Havel, and D. G. Cory, Phys. Rev. A **61**, 012302 (2000).

[18] A. K. Khitrin and B. M. Fung, Phys. Rev. A **64**, 032306 (2001).

[19] Experimental results were anticipated in the Lattice 2001 Conference in Berlin; G. Ortiz, E. Knill, and J. E. Gubernatis, Nucl. Phys. B **106**, 151 (2002). Here we present them in full detail.

[20] M. A. Nielsen and I. L. Chuang, *Quantum Computation and Quantum Information* (Cambridge University Press, Cambridge, UK, 2000).

[21] A. Barenco *et al.*, Phys. Rev. A **52**, 3457 (1995).

[22] D. DiVicenzo, Phys. Rev. A **51**, 1015 (1995).

[23] We actually restrict ourselves to 90° and 180° rotations for experimental calibration issues.

[24] Note that, even though efficient techniques to prepare a pseudopure state exist in theory [25], in practice they are very hard to implement and one instead uses nonefficient methods that suffer a exponential decay of observed signal with respect to the number of qubits in the pseudopure state.

[25] L. Schuman and U. Vazirani, Scalable NMR quantum computation., *Proceedings of the 31st ACM Symposium on Theory of Computing*, 1998, pp. 322–329.

[26] P. Jordan and E. Wigner, Z. Phys. **47**, 631 (1928).

[27] R. Somma, G. Ortiz, E. Knill, and J. Gubernatis, Int. J. Quantum Inf. **1**, 189 (2003).

[28] The Hadamard gate is the single-qubit rotation $ie^{i(\pi/2)\sigma_x}e^{i(\pi/4)\sigma_y}$.

[29] E. Knill, R. Laflamme, R. Martinez, and C. Tseng, Nature (London) **404** 368 (2000).

[30] E. Knill, R. Laflamme, R. Martinez, and C. Negrevergne, Phys. Rev. Lett. **86**, 5811 (2001).

[31] By ideal we mean without experimental error and decoherence effects.

[32] The only effect of spins (C_4, C_3, H_2, H_1) on the other spins is a Larmor frequency shift that can be absorbed into the phase tracking calculation.

[33] See, for example, P. W. Shor, Phys. Rev. A **52**, R2493 (1995); P. W. Shor, in *Proceedings of the 37th Annual IEEE Symposium of Foundaments of Computer Science*, FOC'96 , Burlington, VT (1996), pp. 56–65. A. M. Steane, Phys. Rev. Lett. **77**, 793 (1996); A. Y. Kitaev, Russ. Math. Surveys **52**, 1191 (1997).

[34] Using these techniques would require to achieve an error-rate per gate below a threshold value depending on the exact error correction method used. Although none of these correcting techniques have been used in the present work, quantum error correction codes have been successfully implemented on the same NMR system [30].

[35] Only a discrete set of frequencies can be obtained from the evaluation of the DFT over a discrete sample $[S(t_j)]$. In this case, a (Nyquist) critical frequency is given by $\eta_c = 2\pi/\Delta t$ such that if $S(t)$ contains frequencies greater than η_c, they will not be obtained by applying a DFT (sampling theorem). Notice that two different frequencies η_l and $\eta_{l'}$ are equivalent in a DFT whenever they differ by an integer number of η_c: $\eta_l \equiv \eta_{l'} \Leftrightarrow \eta_l = \eta_{l'} + p\,\eta_c$, with p an integer number.

[36] Due to experimental errors, the imaginary part of $\tilde{S}(\eta_l)$ could be in principle different from zero. However, we consider only its real part because it contains all the desired information (e.g., eigenvalues).

[37] J. Taylor, *An Introduction to Error Analysis* (University Science Books, Sausalito, CA, 1997).